

Compact SQUID realized in a double layer graphene heterostructure

David I. Indolese,^{*,†} Paritosh Karnatak,[†] Artem Kononov,[†] Raphaëlle Delagrangé,[†]
Roy Haller,[†] Lujun Wang,^{†,‡} Péter Makk,[¶] Kenji Watanabe,[§] Takashi Taniguchi,^{||}
and Christian Schönenberger^{†,‡}

[†]*Department of Physics, University of Basel, Klingelbergstrasse 82, CH-4056 Basel,
Switzerland*

[‡]*Swiss Nanoscience institute, University of Basel, Klingelbergstrasse 82, CH-4056 Basel,
Switzerland*

[¶]*Department of Physics, Budapest University of Technology and Economics and
Nanoelectronics Momentum Research Group of the Hungarian Academy of Sciences,
Budafoki ut 8, 1111 Budapest, Hungary*

[§]*Research Center for Functional Materials, National Institute for Material Science, 1-1
Namiki, Tsukuba 305-0044, Japan*

^{||}*International Center for Materials Nanoarchitectonics, National Institute for Material
Science, 1-1 Namiki, Tsukuba 305-0044, Japan*

E-mail: david.indolese@unibas.ch

Abstract

Two-dimensional systems that host one-dimensional helical states are exciting from the perspective of scalable topological quantum computation when coupled with a superconductor. Graphene is particularly promising for its high electronic quality, versatility in van der Waals heterostructures and its electron and hole-like degenerate $0th$

Landau level. Here, we study a compact double layer graphene SQUID (superconducting quantum interference device), where the superconducting loop is reduced to the superconducting contacts, connecting two parallel graphene Josephson junctions. Despite the small size of the SQUID, it is fully tunable by independent gate control of the Fermi energies in both layers. Furthermore, both Josephson junctions show a skewed current phase relationship, indicating the presence of superconducting modes with high transparency. In the quantum Hall regime we measure a well defined conductance plateau of $2e^2/h$ an indicative of counter propagating edge channels in the two layers. Our work opens a way for engineering topological superconductivity by coupling helical edge states, from graphene's electron-hole degenerate $0th$ Landau level via superconducting contacts.

The coupling of one-dimensional (1D) helical states to a superconductor is expected to generate zero energy Majorana bound states.¹⁻³ Currently, the most popular approach to engineer Majorana zero modes is to use 1D semiconducting nanowires with large spin orbit coupling in contact with a superconductor exposed to large magnetic fields (B).⁴⁻⁷ However, two-dimensional (2D) systems are required to realise scalable architectures for topological quantum computation, and some efforts have been made in this direction using semiconducting quantum well structures.⁸⁻¹¹ Nevertheless, these materials are difficult to fabricate and often suffer from a bulk contribution to the current transport.^{12,13} Graphene, on the other hand, exhibits extremely high electronic quality and can be assembled into versatile heterostructures along with other van der Waals (vdW) materials to create novel device characteristics.¹⁴

Graphene, by itself, is neither a topological insulator nor possesses helical states at $B = 0$. However, it can be used in vdW heterostructures to engineer helical states. Previous experiments have shown the manifestation of this state by applying a large tilted magnetic field up to 30 T to increase the Zeeman energy,¹⁵ by gating large angle twisted bilayer graphene to opposite filling factors of ± 1 ,¹⁶ or by using SrTiO₃ with its large dielectric constant as a substrate to screen the long range Coulomb interactions.¹⁷ All these approaches

rely on the electron and hole-like, four fold (spin and valley) degenerate $0th$ Landau level (LL) in graphene. In the quantum Hall (QH) regime, the ground state at charge neutrality is determined by the splitting of the four-fold degenerate LLs into spin or valley polarised states, which depend on the details of the interaction terms.¹⁸⁻²² The other necessary component for topological superconductivity is the coupling of the helical states to a superconductor in such a way, that an electron (hole) propagating forward in one channel is reflected as a hole (electron) propagating backwards in the other. In a system where two layers of graphene are placed one on top of the other, this can be achieved with crossed Andreev reflections (CAR)²³. This has been shown to be possible at $B=0$ if the two layers are closer than the superconducting coherence length of the electrodes.²³ Combined with the possibility of inducing superconducting correlations in graphene QH edge states,^{24,25} an engineered topological superconductivity should be experimentally accessible.

In this work, we investigate Josephson junction made from a vdW heterostructure with two graphene layers separated by a thin hexagonal boron nitride (hBN) crystal. In the QH regime, we gate the two layers to the filling factors of ± 1 , which are states with opposite spin and propagation direction¹⁶ (see Fig.1 a). This mimics an artificial 1D helical conductor and manifests as a well defined conductance plateau of $2e^2/h$, where h is the Planck constant and e the elementary charge. Superconducting molybdenum-rhenium (MoRe) side contacts, with a critical magnetic field B_c of ~ 8 T, connect the double layer graphene (DLG) forming two parallel MoRe-graphene-MoRe Josephson junctions (JJ) as shown in Fig.1 b. As a whole, it constitutes a compact SQUID whose superconducting loop is reduced to the electrodes. The critical current (I_c) in both JJs can be independently tuned to define a symmetric or an asymmetric SQUID. In the later case, we measure the current phase relation (CPR) of both graphene JJs and observe superconducting modes with a high transparency. Demonstrating helical edge modes in two graphene layers placed within a superconducting coherence length of each other represents our first step towards engineering topological superconductivity in graphene based heterostructures.

We fabricated six-layered vdW heterostructures shown in Fig.1 b by a standard polycarbonate assisted pick-up technique.²⁶ The hBN between the graphene sheets, has three atomically defined thicknesses - 12 nm, 25 nm and 50 nm for junctions J_1 , J_2 and J_3 respectively. The self-aligned MoRe side contacts were sputtered after etching the contact region with CHF_3/O_2 .²⁷ The hBN on the bottom and top were used as gate dielectrics. Aluminium oxide (Al_2O_3) with a thickness of 30 nm was grown by atomic layer deposition to electrically insulate the top gate from the contacts as well as from the etched edges of the stack, which define the mesa. A scanning electron microscope image of the top view and a cut made by a focused ion beam are shown in Fig.1 b. The fabrication details can be found in the SI.

First we characterise the junctions by measuring the normal state resistance (R_n), which is shown for J_2 , in Fig.1 c and for all three junctions in the SI. It was measured at a constant voltage bias of 4 mV, which is well above 2Δ , where $\Delta=1.3$ meV is the superconducting gap of MoRe.²⁸ At this voltage bias, the current is carried by quasi particles and any influence of the superconducting contacts can be neglected. The electron densities of the top (n_t) and the bottom (n_b) layer are calculated by an electrostatic model for each pair of top (V_{tg}) and back gate (V_{bg}) voltage (see SI). Two clear lines of enhanced resistance at n_t and n_b equal to zero, correspond to the Dirac points (DP) of the individual layers, and split the $R_n(n_b, n_t)$ into four quadrants. We observe the highest mean resistance in the quadrant, where both layers are hole (p) doped, resulting from the workfunction mismatch between graphene and MoRe, which electron (n) dopes the graphene near the contacts.²⁹ This pn junction at both electrodes leads to a charge carrier dependent reflection probability, i.e. Fabry-Pérot oscillations, if the phase coherence length is larger than the junction length (L).^{29,30} For a higher visibility of the oscillations, the derivatives of R_n with respect to n_b and to n_t are shown in Fig.1 c. The mobility (μ) and the contact resistance (R_c) are determined from the charge carrier dependent conductivity σ for $n_t = 0$ and $n_b = 0$ (see SI). The relatively high μ values up to 53'000 cm^2/Vs and the observation of Fabry-Pérot oscillations indicate ballistic transport in both junctions.

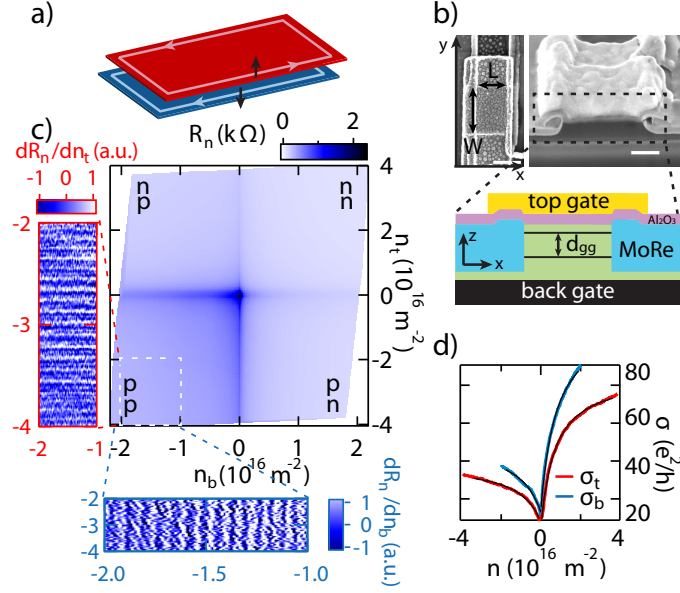


Figure 1: a) Schematic of a DLG device in the QH regime, where the top (bottom) graphene layer is indicated in red (blue) and at a filling factor of $+1$ (-1). The edges states are spin polarized and together form a helical QH state. b) SEM images of a DLG JJ with a schematic of the cross-section. The image on the top left shows the top view of J_1 lying in the xy -plane with a length of 580 nm and a width $1 \mu\text{m}$. Scale bar is 500 nm . On the right a cross-section of the J_1 with a d_{gg} of 12 nm . The sample is cut parallel to the x axis. Scale bar represents 200 nm . The schematics on the bottom shows a sketch of the cross-section. The thin (thick) black lines corresponds to the graphene (graphite gate), the green areas to the hBN, blue to the MoRe contacts, pink to the Al_2O_3 and yellow to the gold top gate. c) Normal state resistance (R_n) of J_2 as a function of top and bottom carrier density. The red (blue) framed graph shows the derivative of R_n in the white dashed enclosed region with respect to n_t (n_b). d) Cuts of the R_n measurements at $n_t = 0$ (blue) and $n_b = 0$ (red) are shown. The black lines are fits of the conductivity as a function of n given by the mobility and contact resistance.

To explore the presence of the engineered helical state in our junctions, we measure the device conductance (G) in an out-of-plane B of 5 T (see Fig.2 a). We observe well defined conductance plateaus as a function of V_{tg} and V_{bg} . In the QH regime the current is carried by a discrete number of edge channels, which is given by the filling factor ν .³¹ For electrically separated DLG, there is no coupling of edge channels, and G of each plateau is given by the sum of the absolute filling factors in both layers, $G = \frac{e^2}{h} (|\nu_b| + |\nu_t|)$ with $\nu_i = \pm 2, \pm 6, \pm 10, \dots$, where i is the index for the bottom or the top layer, assuming that the four fold degeneracy of each LL is not lifted.

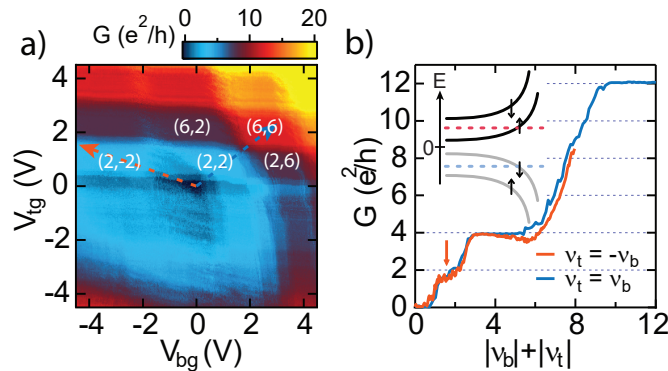


Figure 2: a) Conductance as a function of top and back gate. Clear plateaus of constant conductance and a degeneracy lifting of the $0th$ Landau level are observed. The white numbers indicate some filling factors in the top (left number) and bottom (right number) graphene layer for the conductance plateau. b) Cuts of the conductance map shown in a) along equal $n_b = n_t$ (blue) and opposite $n_b = -n_t$ with $n_t > 0$ (orange) as a function of the sum of the absolute filling factors. Inset: Energy spectrum of the $0th$ Landau level for a single layer graphene with spin and valley degeneracy lifted. The black (gray) lines correspond to electron (hole) like states. The chemical potential of the top graphene (red dashed line) is set between the filling factors of $\nu = 1$ and 2 . The blue dashed line indicates the position of the chemical potential of the bottom graphene set between $\nu = -1$ and -2 . This situation corresponds to the conductance plateau pointed at by the orange arrow.

For equal charge carrier density in both layers, one expects a sequence of $\nu_{tot} = |\nu_b| + |\nu_t| = 4, 12, 20, \dots$, when neither of the degeneracy, i.e. spin or valley, is lifted. In Fig.2 b the blue curve corresponds to the cut along $\nu_t = \nu_b$, where the edge channels in the two graphene layers are electron like and propagate in the same direction. We observe plateaus with $4 \frac{e^2}{h}$, $12 \frac{e^2}{h}$ and $20 \frac{e^2}{h}$ as expected. Exceptionally, an additional plateau with $G = 2 \frac{e^2}{h}$ exists, which

appears due to the lifting of the degeneracies of the $0th$ LL by many-body correlation.³² The same value in conductance is also observed for $\nu_t = -\nu_b$ with $\nu_t > 0$. In this case the n-doped top layer and the p-doped bottom layer host counter propagating edge channels. The presence of an insulating ground state at charge neutrality indicates the lifting of the valley and spin degeneracy such that edge channels for $\nu = 1$ and $\nu = -1$ must be spin polarized with opposite spins, and form a 1D helical state¹⁶. While the MoRe is still superconducting at 5 T, we do not observe superconducting pockets²⁴ for $\nu_{t/b} = \pm 1$, even when the ac-current modulation was reduced to 50 pA.

Next, we characterise the superconducting properties of our junctions at $B = 0$, which is shown in Fig.3 for J_2 . Here, I_c was measured as a function of n_t and n_b (see Fig.3 a) by the appearance of a non-zero trigger voltage (V_{trig}) over the junction, while sweeping the bias current (as detailed in SI). The observed smallest I_c is of around 40 nA at $n_t = n_b = 0$. The critical current of the bottom (top) layer I_c^b (I_c^t) extracted at $n_t = 0$ ($n_b = 0$) shows a similar dependence of n_b (n_t) as the conductivity (see Fig.3 b), as expected from the Ambegaokar-Baratoff relation ($R_n I_c \propto \Delta$).³³ Here, the superconducting coherence length in graphene $\xi_g = \frac{\hbar v_F}{\pi \Delta} = 160$ nm, where \hbar is the reduced Plank constant and v_F is the Fermi velocity of graphene, is smaller than L . For such a long junction ($\xi_g < L$) the product of R_n and I_c is proportional to the Thouless energy³⁴ instead of Δ (see SI).

A magnetic flux $\Phi_z = \Phi(B_z)$, induced by an out-of plane magnetic field B_z threading through a planar JJ creates a phase difference between the superconducting trajectories. That results in an interference pattern, which is measured as the dependence of I_c with respect to B_z , obtained by sweeping a dc-current with an added ac-modulation of 10 nA and detecting the differential resistance (see Fig.3 c). If the current distribution is homogeneous along the y-axis, I_c can be expressed as a function of B_z as,³⁵

$$I_c(B_z) = I_c(0) \left| \frac{\sin(\pi \Phi(B_z)/\Phi_0)}{\pi \Phi(B_z)/\Phi_0} \right|, \quad (1)$$

where Φ_0 is the magnetic flux quantum given by $h/2e$ and $\Phi_z = W(L + 2\lambda)B_z$ ³⁵ with

$\lambda \approx 150$ nm equal to the London penetration depth of MoRe. Since the measured I_c describes a Fraunhofer like interference pattern, we conclude that the supercurrent density is indeed homogeneous in both layers. The period of the oscillation in B_z matches the sample dimensions. Note, that $I_c(B_z)$ drops to zero within a small field of 10 mT.

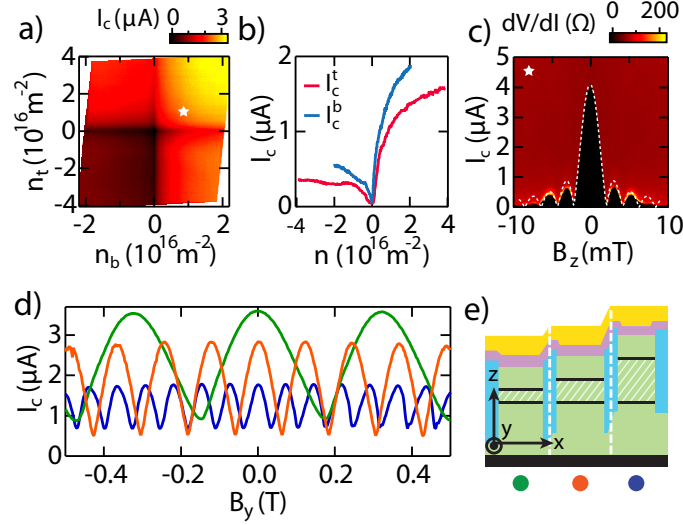


Figure 3: a) I_c as a function of n_t and n_b . b) Cuts along $n_t = 0$ (blue) and $n_b = 0$ (red). c) Interference pattern of the DLG JJ as a function of out-of-plane magnetic field B_z . The white star in Fig.3a indicates the position in n_b and n_t , where the interference pattern is measured. The interference pattern is overlaid with a Fraunhofer interference pattern (white dashed line) given by Eq.1. d) Interference pattern of DLG JJ as a function of in-plane magnetic field B_y . The different colors correspond to different d_{gg} . e) Schematic cross-section of the different JJ. The coloured dots are related to the interference pattern in d). The flux through the striped areas has to be considered to calculate the period in magnetic field.

The measurements shown in Fig.3a & c can not distinguish between the current that flows in the top or the bottom layer of the DLG JJs. In contrast, the in-plane magnetic field B_y (y-axis) dependence of I_c is sensitive to the relative magnitude of I_c in both junctions. For this measurement, the alignment of B is crucial (see SI), since a small out-of-plane component leads to a fast decay of I_c as we have seen before (see Fig.3c). The magnetic flux Φ_y , given by B_y – threading through the loop formed by the two vertically stacked graphene layers and the superconducting electrodes, induces a phase difference between the two JJs, given by $\varphi_t = \varphi_b + \frac{2\pi\Phi_y}{\Phi_0}$, where φ_i is the phase difference over the i-th JJ. In general, the

total supercurrent (I_s) of the SQUID is given by

$$I_s(\varphi_t, \varphi_b) = I_c^t g^t(\varphi_t) + I_c^b g^b(\varphi_b), \quad (2)$$

where g^i is the CPR of the i -th JJ and thereby an odd 2π periodic function. In the case of JJ with a tunnel barrier as a weak link, $g(\varphi) = \sin(\varphi)$. As mentioned, φ_t can be replaced by $\varphi_b + \frac{2\pi\Phi_y}{\Phi_0}$ in Eq.2. The critical current as a function of Φ_y is then obtained by maximizing $I_c(\varphi_b, \Phi_y)$ over φ_b for a given B_y .

$$I_c(\Phi_y) = \max_{\varphi_b} \left\{ I_c^t g^t \left(\varphi_b + \frac{2\pi\Phi_y}{\Phi_0} \right) + I_c^b g^b(\varphi_b) \right\}, \quad (3)$$

The measurements for all three SQUIDs show an expected $|\cos(\pi\Phi_y/\Phi_0)|$ like behavior (see Fig.3 d), for a symmetric SQUID configuration, i.e. when $I_c^t \approx I_c^b$ ³⁶ and an assumed sinusoidal CPR. From the periodicity of the interference pattern in B_y we extract the cross sectional area $L \times d_{gg}$, for which we obtain a good agreement with their physical dimensions [J₁: (580 nm×12 nm, J₂: (650 nm×25 nm, J₁: (530 nm×50 nm)]. Note, that the minimal value of I_c never reaches zero, revealing either a small difference between the critical currents of both layers or a non-sinusoidal CPR of the junctions. In the SI we show that even for $I_c^t = I_c^b$ the total I_c does not go to zero. We observe no signs of a CAR contribution with a period of h/e , which would alter the value of every second maxima, although the d_{gg} is on the order of ξ_{MoRe} .³⁷ Another possibility is the momentum mismatch between the two graphene layers by a twist angle.¹⁶

Finally we characterise each JJ by measuring the CPR employing the high individual tunability of I_c^t & I_c^b . The CPR gives an insight into the Cooper pair transport across the junction, e.g. transparency of Andreev bound states. For I_c^b much larger than I_c^t ($\frac{I_c^b}{I_c^t} \geq 10$), φ_b can be assumed constant in Eq.3 such that f^b stays at its maximum value. This results in $I_c = I_c^b + I_c^t g^t(\varphi_b^{max} - \frac{2\pi\Phi}{\Phi_0})$.³⁸ In this case a change in flux leads to an oscillation around I_c^b with an amplitude of $\pm I_c^t$, while the shape of the oscillation is given by g^t . Hence, by using

an asymmetric configuration the CPR can be obtained.

For the sake of clarity, we discuss the CPR for a JJ in the short junction limit. Here, the CPR is determined by the number of transport channels and their transparencies. The critical current of a short JJ is then given by

$$I_c = \frac{e\Delta}{2\hbar} \sum_n \frac{t_n \sin(\varphi)}{\sqrt{1 - t_n \sin^2(\varphi/2)}}, \quad (4)$$

where t_n is the transparency of the n-th channel.^{39–41} For a superconducting tunnel junction, one expects a sinusoidal CPR since only channels with low transparency ($t_n \ll 1$) contribute to transport. If the channel transparencies increase the maximum of the CPR starts to deviate from $\varphi_{max} = \pi/2$ towards π .^{42–45} This deviation is quantified by the skewness of the CPR, defined as $S = \frac{\varphi_{max} - \pi/2}{\pi/2}$.⁴⁴ The skewness is 0, when the CPR is sinusoidal ($t_n \ll 1$), and is 1 when the CPR is sawtooth like ($t_n = 1$). Note, that S and t_n have a non-linear relation, such that a single channel with $t=0.9$ causes only a skewness of 0.35.

In Fig.4 a we show the results of the CPR measurements around the DPs. The reference junction was highly n doped and has a large I_c ($I_c^t \approx 1.5 \mu A$ & $I_c^b \approx 2 \mu A$). Four examples of the CPR at different densities are shown in Fig.4 b. The positions in n_b are indicated in Fig.4 a. A strong decrease of the amplitude at the DP is observed (orange). For values of $n_b \neq 0$ we observe a skewed sinusoidal like oscillation. To extract the skewness, the measurement data were fitted over six periods by using,

$$I_c^i = \sum_{n=1}^5 a_n \sin(nf \times (B_y + B_0)), \quad (5)$$

where a_n is the pre-factor of the n-th harmonic, f the frequency of the oscillations, and B_0 the shift in B_y with respect to the first zero crossing of the oscillation. The pre-factors and their ratio is shown in the SI. The skewness, extracted from the maximum of the fit at each $n_{t/b}$, is plotted in Fig.4 c. The largest $S \approx 0.25$ was observed when the layers are n doped. For the p doped graphene a S of around 0.15 was deduced from the data. By

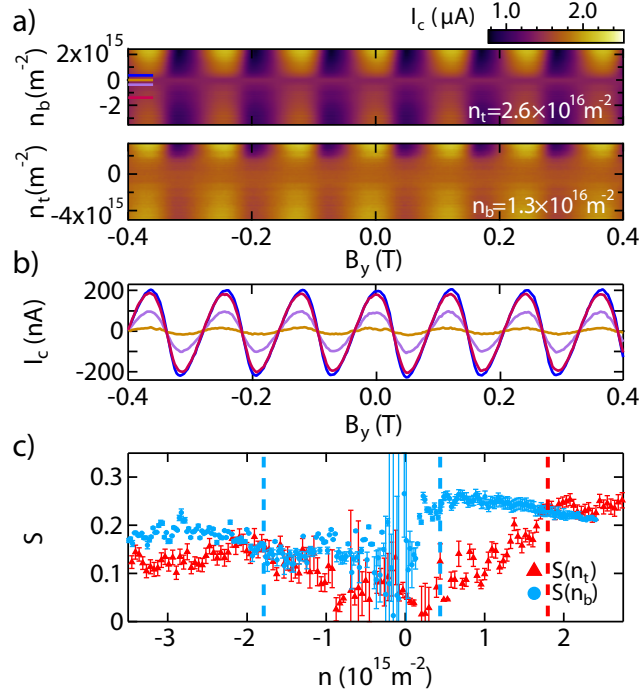


Figure 4: a) Interference pattern as a function of n_b (top) respectively n_t (bottom) and in-plane magnetic field for fixed top respectively bottom charge carrier density. b) Cuts of the interference pattern as a function of B_y for different n_b after subtracting the critical current of the reference junction. The color of the curves corresponds to the color of the bars at the left axis of the top graph in a), which indicates the positions in n_b where the line cuts are taken. c) The skewness of the CPR as a function of n_b (blue) and n_t (red) are shown. The blue (red) dashed line corresponds to a ratio of I_c^b/I_c^t (I_c^t/I_c^b) equal to 0.15.

assuming a single channel in the short junction limit, these values would correspond to a transparency of $t = 0.7$ for $S = 0.25$ and $t = 0.6$ for $S = 0.15$ in Eq.4. Towards the DPs we observe a reduction of the skewness, which indicates that the transparency of the modes reduces when compared to higher doping. $S(n_b)$ also appears to decrease at large electron density, but is possibly due to the assumption $\frac{I_c^b}{I_c^e} \gg 1$ breaking down. The interference signal rapidly diminishes for densities lower than $2 \times 10^{14} \text{ m}^{-2}$. This corresponds to a wavelength $\lambda_F \approx 250 \text{ nm}$ comparable to the length of the junction. For $L < \lambda_F$, the remaining modes have an angle and will be suppressed at the pn-junction that appear close to the contacts. This explains the rapid reduction in the I_c and the sinusoidal CPR close to the DPs.

We note, that the self inductance L_s of the SQUID can also lead to a non-linear dependence of φ as a function of B caused by screening of the external magnetic field by the current in the SQUID loop.⁴⁰ This effect is especially dominant around $\Phi = \Phi_0/2$, where the current in the loop is the largest and can mimic a non-sinusoidal CPR. However, in our compact DLG SQUID, the weak links (i.e. the graphene layers) are intersected by two short superconducting segments. This results in a negligible contribution from the kinetic inductance irrespective of the superconducting material and also a minimal geometrical inductance (see SI), in contrast to a regular SQUID geometry.

In conclusion, we engineer a helical state in a double layer graphene van der Waals heterostructure using the unique properties of the 0th LL of graphene. This is reflected by the observation of a well defined conductance plateau of $2e^2/h$, when each of the two layers hosts an opposite chirality edge channel, i.e. for $\nu_t = -\nu_b$ with $|\nu_t| = 1$. We show that the supercurrent is carried by both layers and the critical currents are individually tunable and show a strong carrier density dependence. The measurement of the current phase relation reveals the high transparency in both graphene Josephson junctions. Further, the loop inductance of such a compact SQUID is negligible in interference measurements. We do not observe crossed Andreev reflection between the two graphene layers possibly due to the short coherence length of MoRe or a momentum mismatch between the two misaligned

layers. Our graphene based heterostructure, however, allows a small interlayer spacing and the alignment of the crystal axes of the graphene layers by the tear and stack technique,⁴⁶ which paves the way for future experiments to couple the helical quantum Hall edge states by crossed Andreev reflection.

Acknowledgement

The authors acknowledge the support by the Swiss Nanoscience Institute (SNI), the ERC project TopSupra (787414), the European Union Horizon 2020 research and innovation program under grant agreement No. 785219 (Graphene Flagship), the Swiss National Science Foundation and the Swiss NCCR QSIT. A.K. was supported by the Georg H. Endress foundation. Topograph FlagERA network, OTKA FK-123894. This research was supported by the National Research, Development and Innovation Fund of Hungary within the Quantum Technology National Excellence Program (Project Nr. 2017-1.2.1-NKP-2017-00001). P.M. acknowledges support from the Marie Curie and Bolyai fellowships. K.W. and T.T. acknowledge support from the Elemental Strategy Initiative conducted by the MEXT, Japan ,Grant Number JPMXP0112101001, JSPS KAKENHI Grant Numbers JP20H00354 and the CREST(JPMJCR15F3), JST. D.I. acknowledges the fruitful discussions with Simon Zihlmann.

Author contributions

D.I, P.M, R.D. and C.S. conceived the experiment. D.I. did the fabrication of the device with the input of L.W. The measurements were performed by D.I. with the input of P.K and A.K. The hBN crystals was provided K.W. and T.T. R.H. maintained the measurement setup and improved it together with D.I. Further D.I. analysed the data with inputs of P.K. and A.K. D.I. and P.K. wrote the manuscript with contribution from all authors.

Supporting Information Available

The following files are available free of charge.

The following files are available free of charge.

- Supporting Informations: Compact SQUID realized in a double layer graphene heterostructure: Detailed description of device fabrication, experimental methods and complementary measurements
- All measurement data in this publication are available in numerical form (DOI:10.5281/zenodo.388669)

References

- (1) San-Jose, P.; Lado, J. L.; Aguado, R.; Guinea, F.; Fernández-Rossier, J. Majorana zero modes in graphene. *Physical Review X* **2015**, *5*, 1–15.
- (2) Fu, L.; Kane, C. L. Superconducting proximity effect and majorana fermions at the surface of a topological insulator. *Physical Review Letters* **2008**, *100*, 1–4.
- (3) Alicea, J. Majorana fermions in a tunable semiconductor device. *Physical Review B - Condensed Matter and Materials Physics* **2010**, *81*, 1–10.
- (4) Mourik, V.; Zuo, K.; Frolov, S. M.; Plissard, S. R.; Bakkers, E. P.; Kouwenhoven, L. P. Signatures of majorana fermions in hybrid superconductor-semiconductor nanowire devices. *Science* **2012**, *336*, 1003–1007.
- (5) Das, A.; Ronen, Y.; Most, Y.; Oreg, Y.; Heiblum, M.; Shtrikman, H. Zero-bias peaks and splitting in an Al-InAs nanowire topological superconductor as a signature of Majorana fermions. *Nature Physics* **2012**, *8*, 887–895.
- (6) Rokhinson, L. P.; Liu, X.; Furdyna, J. K. The fractional a.c. Josephson effect in a semiconductor-superconductor nanowire as a signature of Majorana particles. *Nature Physics* **2012**, *8*, 795–799.

- (7) Suominen, H. J.; Danon, J.; Kjaergaard, M.; Flensberg, K.; Shabani, J.; Palmstrøm, C. J.; Nichele, F.; Marcus, C. M. Anomalous Fraunhofer interference in epitaxial superconductor-semiconductor Josephson junctions. *Physical Review B* **2017**, *95*, 1–11.
- (8) Hart, S.; Ren, H.; Wagner, T.; Leubner, P.; Mühlbauer, M.; Brüne, C.; Buhmann, H.; Molenkamp, L. W.; Yacoby, A. Induced superconductivity in the quantum spin Hall edge. *Nature Physics* **2014**, *10*, 638–643.
- (9) Pribiag, V. S.; Beukman, A. J.; Qu, F.; Cassidy, M. C.; Charpentier, C.; Wegscheider, W.; Kouwenhoven, L. P. Edge-mode superconductivity in a two-dimensional topological insulator. *Nature Nanotechnology* **2015**, *10*, 593–597.
- (10) Fornieri, A. et al. Evidence of topological superconductivity in planar Josephson junctions. *Nature* **2019**, *569*, 89–92.
- (11) Mayer, W.; Dartiailh, M. C.; Yuan, J.; Wickramasinghe, K. S.; Matos-Abiague, A.; Žutić, I.; Shabani, J. Phase signature of topological transition in Josephson Junctions. *arXiv* **2019**, *1906.01179*, 1–11.
- (12) Nowack, K. C.; Spanton, E. M.; Baenninger, M.; König, M.; Kirtley, J. R.; Kalisky, B.; Ames, C.; Leubner, P.; Brüne, C.; Buhmann, H.; Molenkamp, L. W.; Goldhaber-Gordon, D.; Moler, K. A. Imaging currents in HgTe quantum wells in the quantum spin Hall regime. *Nature Materials* **2013**, *12*, 787–791.
- (13) Charpentier, C.; Fält, S.; Reichl, C.; Nichele, F.; Nath Pal, A.; Pietsch, P.; Ihn, T.; Ensslin, K.; Wegscheider, W. Suppression of bulk conductivity in InAs/GaSb broken gap composite quantum wells. *Applied Physics Letters* **2013**, *103*, 28–31.
- (14) Yankowitz, M.; Ma, Q.; Jarillo-Herrero, P.; LeRoy, B. J. van der Waals heterostructures combining graphene and hexagonal boron nitride. *Nature Reviews Physics* **2019**, *1*, 112–125.

- (15) Young, A. F.; Sanchez-Yamagishi, J. D.; Hunt, B.; Choi, S. H.; Watanabe, K.; Taniguchi, T.; Ashoori, R. C.; Jarillo-Herrero, P. Tunable symmetry breaking and helical edge transport in a graphene quantum spin Hall state. *Nature* **2013**, *505*, 528–532.
- (16) Sanchez-Yamagishi, J. D.; Luo, J. Y.; Young, A. F.; Hunt, B.; Watanabe, K.; Taniguchi, T.; Ashoori, R. C.; Jarillo-Herrero, P. Observation of Helical Edge States and Fractional Quantum Hall Effect in a Graphene Electron-hole Bilayer. *Nature Nanotechnology* **2016**, *12*, 118–122.
- (17) Veyrat, L.; Déprez, C.; Coissard, A.; Li, X.; Gay, F.; Watanabe, K.; Taniguchi, T.; Han, Z.; Piot, B. A.; Sellier, H.; Sacépé, B. Helical quantum Hall phase in graphene on SrTiO₃. *Science* **2020**, *367*, 781–786.
- (18) Abanin, D. A.; Lee, P. A.; Levitov, L. S. Spin-filtered edge states and quantum hall effect in graphene. *Physical Review Letters* **2006**, *96*, 1–4.
- (19) Young, A. F.; Dean, C. R.; Wang, L.; Ren, H.; Cadden-Zimansky, P.; Watanabe, K.; Taniguchi, T.; Hone, J.; Shepard, K. L.; Kim, P. Spin and valley quantum Hall ferromagnetism in graphene. *Nature Physics* **2012**, *8*, 550–556.
- (20) Kharitonov, M. Phase diagram for the $\nu=0$ quantum Hall state in monolayer graphene. *Physical Review B - Condensed Matter and Materials Physics* **2012**, *85*, 1–23.
- (21) Herbut, I. F. Theory of integer quantum Hall effect in graphene. *Physical Review B - Condensed Matter and Materials Physics* **2007**, *75*, 1–5.
- (22) Amet, F.; Williams, J. R.; Watanabe, K.; Taniguchi, T.; Goldhaber-Gordon, D. Selective equilibration of spin-polarized quantum hall edge states in graphene. *Physical Review Letters* **2014**, *112*, 1–5.
- (23) Park, G.-H.; Watanabe, K.; Taniguchi, T.; Lee, G.-H.; Lee, H.-J. Engineering Crossed Andreev Reflection in Double-Bilayer Graphene. *Nano Letters* **2019**, *19*, 9002–9007.

- (24) Amet, F.; Ke, C. T.; Borzenets, I. V.; Wang, Y.-M.; Watanabe, K.; Taniguchi, T.; Deacon, R. S.; Yamamoto, M.; Bomze, Y.; Tarucha, S.; Finkelstein, G. Supercurrent in the quantum Hall regime. *Science* **2016**, *352*, 966–969.
- (25) Lee, G. H.; Huang, K. F.; Efetov, D. K.; Wei, D. S.; Hart, S.; Taniguchi, T.; Watanabe, K.; Yacoby, A.; Kim, P. Inducing superconducting correlation in quantum Hall edge states. *Nature Physics* **2017**, *13*, 693–698.
- (26) Zomer, P. J.; Guimaraes, M. H. D.; Brant, J. C.; Tombros, N.; Van Wees, B. J. Fast pick up technique for high quality heterostructures of bilayer graphene and hexagonal boron nitride. *Applied Physics Letters* **2014**, *105*, 1–4.
- (27) Wang, L.; Meric, I.; Huang, P. Y.; Gao, Q.; Gao, Y.; Tran, H.; Taniguchi, T.; Watanabe, K.; Campos, L. M.; Muller, D. A.; Guo, J.; Kim, P.; Hone, J.; Shepard, K. L.; Dean, C. R. One-Dimensional Electrical Contact to. *Science* **2013**, *342*, 614–617.
- (28) Indolese, D. I.; Delagrangé, R.; Makk, P.; Wallbank, J. R.; Watanabe, K.; Taniguchi, T.; Schönenberger, C. Signatures of van Hove Singularities Probed by the Supercurrent in a Graphene-hBN Superlattice. *Physical Review Letters* **2018**, *121*, 137701.
- (29) Calado, V. E.; Goswami, S.; Nanda, G.; Diez, M.; Akhmerov, A. R.; Watanabe, K.; Taniguchi, T.; Klapwijk, T. M.; Vandersypen, L. M. K. Ballistic Josephson junctions in edge-contacted graphene. *Nature Nanotechnology* **2015**, *10*, 761–764.
- (30) Young, A. F.; Kim, P. Quantum interference and Klein tunnelling in graphene heterojunctions. *Nature Physics* **2009**, *5*, 222–226.
- (31) Zhang, Y.; Tan, Y. W.; Stormer, H. L.; Kim, P. Experimental observation of the quantum Hall effect and Berry’s phase in graphene. *Nature* **2005**, *438*, 201–204.
- (32) Zhang, Y.; Jiang, Z.; Small, J. P.; Purewal, M. S.; Tan, Y. W.; Fazlollahi, M.; Chu-

- dow, J. D.; Jaszczak, J. A.; Stormer, H. L.; Kim, P. Landau-level splitting in graphene in high magnetic fields. *Physical Review Letters* **2006**, *96*, 1–4.
- (33) Ambegaokar, V.; Baratoff, A. Tunneling between superconductors. *Physical Review Letters* **1963**, *10*, 486–489.
- (34) Borzenets, I. V.; Amet, F.; Ke, C. T.; Draelos, A. W.; Wei, M. T.; Seredinski, A.; Watanabe, K.; Taniguchi, T.; Bomze, Y.; Yamamoto, M.; Tarucha, S.; Finkelstein, G. Ballistic Graphene Josephson Junctions from the Short to the Long Junction Regimes. *Physical Review Letters* **2016**, *117*, 1–5.
- (35) Tinkham, M. *Introduction to Superconductivity*, 2nd ed.; McGraw-Hill Book CO., 1996.
- (36) Angers, L.; Chiodi, F.; Montambaux, G.; Ferrier, M.; Guéron, S.; Bouchiat, H.; Cuevas, J. C. Proximity dc squids in the long-junction limit. *Physical Review B* **2008**, *77*, 1–12.
- (37) Talvacchio, J.; Janocko, M. A.; Gregg, J. Properties of evaporated Mo-Re thin-film superconductors. *Journal of Low Temperature Physics* **1986**, *64*, 395–408.
- (38) Della Rocca, M. L.; Chauvin, M.; Huard, B.; Pothier, H.; Esteve, D.; Urbina, C. Measurement of the current-phase relation of superconducting atomic contacts. *Physical Review Letters* **2007**, *99*, 1–4.
- (39) Kulik, I. O.; Omel'yanchuk, A. N. Contribution to the microscopic theory of the Josephson effect in superconducting bridges. *JETP Letters* **1975**, *21*, 96–97.
- (40) Golubov, A. A.; Kupriyanov, M. Y.; Il'ichev, E. The current-phase relation in Josephson junctions. *Reviews of Modern Physics* **2004**, *76*, 411–469.
- (41) Spanton, E. M.; Deng, M.; Vaitiekėnas, S.; Krogstrup, P.; Nygård, J.; Marcus, C. M.; Moler, K. A. Current-phase relations of few-mode InAs nanowire Josephson junctions. *Nature Physics* **2017**, *13*, 1177–1181.

- (42) Thompson, M. D.; Ben Shalom, M.; Geim, A. K.; Matthews, A. J.; White, J.; Melhem, Z.; Pashkin, Y. A.; Haley, R. P.; Prance, J. R. Graphene-based tunable SQUIDs. *Applied Physics Letters* **2017**, *110*, 1–4.
- (43) Bretheau, L.; Wang, J. I.-J.; Pisoni, R.; Watanabe, K.; Taniguchi, T.; Jarillo-Herrero, P. Tunnelling spectroscopy of Andreev states in graphene. *Nature Physics* **2017**, *13*, 756–760.
- (44) Nanda, G.; Aguilera-Servin, J. L.; Rakyta, P.; Kormányos, A.; Kleiner, R.; Koelle, D.; Watanabe, K.; Taniguchi, T.; Vandersypen, L. M.; Goswami, S. Current-Phase Relation of Ballistic Graphene Josephson Junctions. *Nano Letters* **2017**, *17*, 3396–3401.
- (45) English, C. D.; Hamilton, D. R.; Chialvo, C.; Moraru, I. C.; Mason, N.; Van Harlingen, D. J. Observation of nonsinusoidal current-phase relation in graphene Josephson junctions. *Physical Review B* **2016**, *94*, 1–7.
- (46) Kim, K.; Yankowitz, M.; Fallahazad, B.; Kang, S.; Movva, H. C.; Huang, S.; Larentis, S.; Corbet, C. M.; Taniguchi, T.; Watanabe, K.; Banerjee, S. K.; Leroy, B. J.; Tutuc, E. Van der Waals Heterostructures with High Accuracy Rotational Alignment. *Nano Letters* **2016**, *16*, 1989–1995.

Supporting Informations: Compact SQUID realized in a double layer graphene heterostructure

David I. Indolese,^{*,†} Paritosh Karnatak,[†] Artem Kononov,[†] Raphaëlle Delagrangé,[†]
Roy Haller,[†] Lujun Wang,^{†,‡} Péter Makk,[¶] Kenji Watanabe,[§] Takashi Taniguchi,^{||}
and Christian Schönenberger^{†,‡}

[†]*Department of Physics, University of Basel, Klingelbergstrasse 82, CH-4056 Basel,
Switzerland*

[‡]*Swiss Nanoscience institute, University of Basel, Klingelbergstrasse 82, CH-4056 Basel,
Switzerland*

[¶]*Department of Physics, Budapest University of Technology and Economics and
Nanoelectronics Momentum Research Group of the Hungarian Academy of Sciences,
Budafoki ut 8, 1111 Budapest, Hungary*

[§]*Research Center for Functional Materials, National Institute for Material Science, 1-1
Namiki, Tsukuba 305-0044, Japan*

^{||}*International Center for Materials Nanoarchitectonics, National Institute for Material
Science, 1-1 Namiki, Tsukuba 305-0044, Japan*

E-mail: david.indolese@unibas.ch

Device fabrication

The fabrication of the van der Waals heterostructure (vdWh), superconducting contacts, and gates is described in the following section. In a first step all the 2D materials, i.e. graphite and hBN, were exfoliated on a silicon wafer with an oxide thickness of 295 nm using the low adhesion tape ELP BT-150P-LC supplied by Nitto. We identified the graphene by the optical contrast difference of 4% in the green channel with respect to the substrate.¹ The thickness of the middle hBN and its plateaus were measured by an atomic force microscope (AFM) using a Bruker Dimension 3100 in tapping mode at ambient conditions.

The stacking of the different crystals was done by a well established technique, which uses a polycarbonate (PC) film on a polydimethylsiloxane (PDMS) pillow.² Here, the such fabricated vdWh consists from bottom to top out of thick graphite, a bottom hBN, a bottom graphene, a middle hBN, a top graphene, and a top hBN flake. Important to mention is that only the top surface of the top hBN flake is in contact with the PC, such that the entire stacking process is fully assisted by the van der Waals forces and it can be considered dry and polymer free. Further the encapsulation protects the graphene layers from contaminations during the device fabrication. In the end the stack was placed at 170 °C on a intrinsic silicon wafer with an oxide thickness of 285 nm. At these temperature the PC detaches fully from the PDMS pillow. The PC residues on top of the stack can be dissolved in dichlormethane for 1 h at room temperature. To clean the top hBN's surface, the stack was annealed at a temperature of 300 °C for 3 h in forming gas (H_2 8%/N₂ 92%) at a background pressure of 20 mbar. This removes remaining PC residues.

During the stacking process it is possible that impurities are trapped between two layers, which manifest themselves in the appearance of bubbles. Using an AFM we can map the clean areas, i.e. the areas without bubbles, which are used for the device fabrication. Further we can determine the thickness of the different hBN, which is important to determine the exact etching times and for the calculation of the electrostatics.

The two layers of graphene have been connected by several common superconducting

edge contacts forming several Josephson junctions (JJs) in series. To fabricate the contacts we used standard electron beam lithography (EBL). A e-beam resist of PMMA 950k, which is dissolved in anisole (concentration of 5.5%), was spin coated with 4000 rpm for 40 s on the sample, resulting in a film thickness of 380 nm. The EBL was performed with an acceleration voltage of 20 kV and a dose of $400 \mu\text{C}/\text{cm}^2$. The resist was developed for 1 min in a IPA/deionized water mixture (7/3) cooled to $\sim 5^\circ\text{C}$ and was then blow dried with nitrogen. To fabricate the superconducting edge contacts the stack was etched by a reactive ion etching using a CHF_3/O_2 plasma with 40 sccm/4 sccm at a background pressure of 60 mTorr and a power of 60 W. The rate of the etching recipe was calibrated in advance to have a very precise control of the amount of etched hBN. This is crucial, since one has to stop the etching process in the bottom hBN layer, such that the bottom gate is electrically insulated from the MoRe electrodes, but both graphene layers can be contacted simultaneously. After the etching, the MoRe was sputtered in a AJA ATC Orion using still the same PMMA mask. For the sputtering we used a target of Mo/Re 1:1, a power of 100 W, a background pressure of 2 mTorr, and a constant Argon flow of 30 sccm. The contacts have a thickness of 80 nm. The lift-off was done in acetone at 50°C . In a next step the MoRe was contacted by Cr/Au (5 nm/125 nm) using another EBL defined mask and electron beam evaporation at a pressure of $5\text{e}^{-7}\text{mbar}$. After the lift-off, an etching mask was prepared by EBL to shape the mesa. To insulate the structure from the topgate it was overgrown by an uniform Al_2O_3 layer of 30 nm using atomic layer deposition (ALD), which involved trimethylaluminium (TMA) and water. We observed that for a homogeneous growth of the Al_2O_3 on the vdWh a short O_2 plasma (flow 16 sccm, pressure 250 mTorr, power 30 W, time 20 s) is needed. This removes remaining polymer residues from the fabrication and leads to a homogeneous wetting of the surfaces. In last step we deposited the metallic topgate.

Normal state resistance

The normal state resistance (R_n) was measured for three different junctions with different inter layer distances (d_{gg}) by applying a bias voltage of 4 mV, which is larger than twice $\Delta_{MoRe} = 1.3$ meV.³ For the junctions with $d_{gg}=12$ nm and 50 nm we observed two Dirac points (DP) as a function of the top gate voltage (V_{tg}) (see Fig.S1 a and c). We attribute this behavior to an inhomogeneous lateral residual doping in the top graphene layer. The splitting of the DP as a function of the back gate voltage (V_{bg}) around charge neutrality (see Fig.S1 a) can then be explained by the density of states (DOS) dependent screening of the top gate by the different top graphene regions. For the junction with a thickness of 25 nm, this behavior is less pronounced, but the DP of the top graphene is broadened in charge carrier density compared to the bottom one, which can be attributed to the same effect.

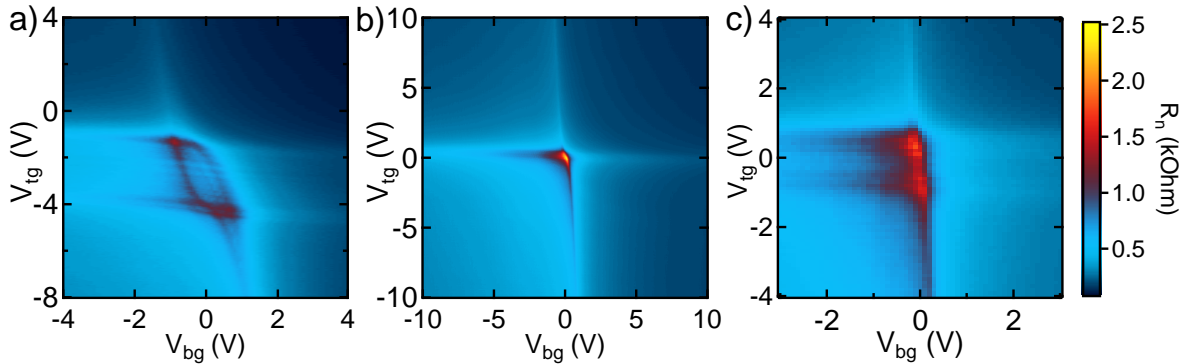


Figure S1: a) Normal state resistance as a function of top and bottom gate for $d_{gg}=12$ nm. b) Normal state resistance as a function of top and bottom gate for $d_{gg}=25$ nm. c) Normal state resistance as a function of top and bottom gate for $d_{gg}=50$ nm.

The Fabry-Pérot cavity length (L_c), i.e. the size of the p doped region, at large n_t and n_b is extracted from the location of neighbouring resistance maxima in charge carrier density using Eq.1.⁴

$$L_c = \frac{\sqrt{\pi}}{\sqrt{n_{i+1}} - \sqrt{n_i}}, \quad (1)$$

where n_i is the position in carrier density of the i -th peak in resistance. We obtain a length

of around 550 nm. The comparison to $L=650$ nm of J_2 indicates that the n doped region at each contact is of the order of 50 nm for large densities.

To extract the mobility μ and contact resistance R_c of J_2 we fit the conductivities, which are plotted in the article in Fig.1 d, by:

$$\sigma^{-1} = \frac{1}{e\mu n + \sigma_0} + \rho_c, \quad (2)$$

where σ_0 is the residual conductivity at the DP, and ρ_c is the contact resistivity. From the fit we obtain an electron mobility of around 53'000 cm²/Vs (33'000 cm²/Vs) and a hole mobility of around 27'000 cm²/Vs (14'000 cm²/Vs) for the bottom (top) graphene. An R_c of 170 Ω (190 Ω) and 440 Ω (490 Ω) is extracted for the bottom (top) graphene for the n-doping and the p-doping, respectively.

Electrostatic model

The charge carrier density in the top (n_t) and the bottom (n_b) graphene were calculated from V_{tg} and V_{bg} using the electrostatic model described in the following section. The structure, which we consider is a DLG (see Fig.S2), consisting of the following layers listed from bottom to top: 1) graphite bottom gate 2) bottom hBN 3) bottom graphene layer 4) middle hBN 5) top graphene layer 6) top hBN 7) aluminium oxide 8) metal top gate.

The top gate is electrically separated from the top graphene by an aluminium oxide layer with a thickness of $d_{Al_2O_3}$ and a dielectric constant $\epsilon_r^{Al_2O_3} = 9.1$ and the top hBN with a thickness of d_t and $\epsilon_r^{hBN} = 4$. A hBN with a thickness of d_{gg} between the two graphene sheets electrically disconnects the two layers, which are shorted at two common 1D edge contacts. hBN was also used as a dielectric material between the bottom graphene plus electrodes and the bottom gate. The thickness of the bottom hBN layer is given by d_b . Since the two graphene layers are electrically shorted, they are at the same electro-chemical potential, which is chosen to be equal to zero, i.e. ground, for the following calculation. From this

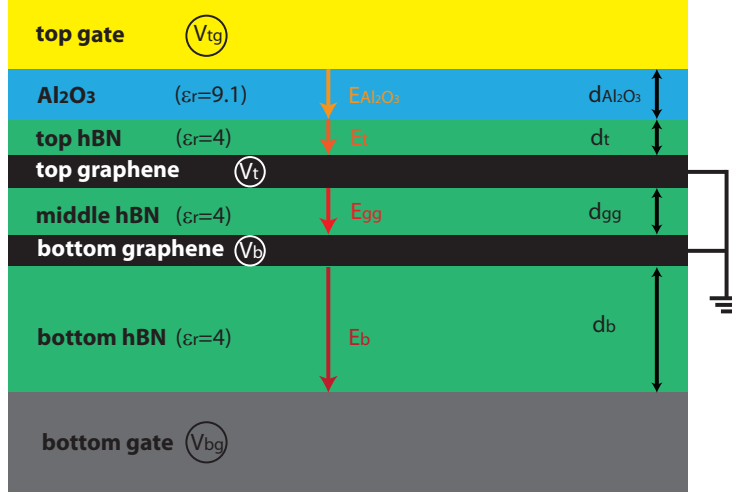


Figure S2: Schematic side view of the DLG stack. The different layers are labelled with its dielectric constant, electric potential and thickness. The arrows define the direction of the electric fields, which was taken for the calculation.

follows that,

$$\mu_c^t - eV_t = \mu_c^b - eV_b = 0, \quad (3)$$

where μ_c^t , μ_c^b are the chemical potential and V_t , V_b are the electrostatic potential of the top, respectively the bottom graphene and e is the elementary charge. For graphene the chemical potential is given as,

$$\mu_c^i = \text{sgn}(n_i) \hbar v_F \sqrt{\pi |n_i|}, \quad (4)$$

where n_i the charge carrier density in the i -th graphene layer. The $\text{sgn}(n_i)$ function is such that it is positive for electron doped and negative for hole doped graphene.

To describe the electrostatic situation we look carefully at the electric fields E_i , where the index i denotes the different dielectrics, which are a consequence of applied gate voltages, quantum capacitance and charge carrier density on either graphene. The electric fields are defined as shown in Fig.S2. In a first step we express $E_{Al_2O_3}$ in terms of E_t . If we consider the interface between the two dielectric materials to be charge free, it follows directly from the

Maxwell equations that normal components of the two electric fields times their dielectric constant have to be the same at the interface. In this case $E_{Al_2O_3}$ is given by,

$$E_{Al_2O_3} = \frac{\epsilon_r^{hBN}}{\epsilon_r^{Al_2O_3}} E_t. \quad (5)$$

Using Gauss law we can write down n_t and n_b as a function of the electric fields.

$$-en_t = \epsilon_0 \epsilon_r^{hBN} (E_{gg} - E_t) \quad (6)$$

$$-en_b = \epsilon_0 \epsilon_r^{hBN} (E_b - E_{gg}), \quad (7)$$

where the vacuum permittivity is given as $\epsilon_0 = 8.854 \times 10^{-12} F/m$. Further the electric fields are given by the voltage differences between the layers and leads to the following sets of equations:

$$E_b d_b = V_b - V_{bg} \quad (8)$$

$$E_{gg} d_{gg} = V_t - V_b \quad (9)$$

$$E_t d_t + E_{Al_2O_3} d_{Al_2O_3} = V_{tg} - V_t. \quad (10)$$

The magnitude of the electric field between the two graphene sheets follows from Eq.9 and 3:

$$E_{gg} = \frac{V_t - V_b}{d_{gg}} = \frac{\sqrt{\pi} \hbar v_F}{e d_{gg}} \left(\text{sgn}(n_t) \sqrt{|n_t|} - \text{sgn}(n_b) \sqrt{|n_b|} \right). \quad (11)$$

From Eq.8 we obtain that $V_{bg} = V_b - E_b d_b$, while E_b can be expressed as a function of n_b and E_{gg} using Eq.7. Therefore it follows that $V_{bg}(n_t, n_b)$ is given as,

$$\begin{aligned}
V_{bg} &= V_b + d_b \left(\frac{en_b}{\epsilon_0 \epsilon_r^{hBN}} - E_{gg} \right) \\
&= \frac{\text{sgn}(n_b) \sqrt{\pi} \hbar v_F}{e} \sqrt{|n_b|} + \frac{en_b d_b}{\epsilon_0 \epsilon_r^{hBN}} - \frac{\sqrt{\pi} \hbar v_F d_b}{e d_{gg}} \left(\text{sgn}(n_t) \sqrt{|n_t|} - \text{sgn}(n_b) \sqrt{|n_b|} \right). \tag{12}
\end{aligned}$$

The same can be done for $V_{tg} = V_t + E_t d_t + E_{Al_2O_3} d_{Al_2O_3}$ starting from Eq.10. By using the relation between the two electric fields one obtains that,

$$V_{tg} = V_t + E_t \left(d_t + \frac{\epsilon_r^{hBN}}{\epsilon_r^{Al_2O_3}} d_{Al_2O_3} \right) \tag{13}$$

For simplification we define $d_t^{eff} = d_t + \frac{\epsilon_r^{hBN}}{\epsilon_r^{Al_2O_3}} d_{Al_2O_3}$. Again we can replace E_t with Eq.6 and in the end we obtain the result,

$$V_{tg} = \frac{\text{sgn}(n_t) \sqrt{\pi} \hbar v_F}{e} \sqrt{|n_t|} + \frac{en_t d_t^{eff}}{\epsilon_0 \epsilon_r^{hBN}} - \frac{\sqrt{\pi} \hbar v_F d_t^{eff}}{e d_{gg}} \left(\text{sgn}(n_b) \sqrt{|n_b|} - \text{sgn}(n_t) \sqrt{|n_t|} \right). \tag{14}$$

Eq.12 and 14 are giving the relation between the gate voltages and the charge carrier densities. To obtain now the charge carrier densities for two given voltages the equations were inverted numerically.

Measurement of I_c

I_c was measured using a FCA3000 counter. The appearance of a finite voltage (V_{trig}) over the junction was triggered, while sweeping the bias current. The value of V_{trig} was set to $6\mu\text{V}$ to be able to measure I_c in the entire gate range, e.g. small I_c at the DP, since the smallest detectable value is given by $I_c^{min} = \frac{V_{trig}}{R_n^{DP}} = 2.5 \text{ nA}$. This small trigger voltage makes the measurement sensitive to voltage noise, which can lead to a trigger error and results in a reduced value for I_c . Due to this, the maximum value of hundred measurements of the stochastic switching current is taken, which deviates not more than 10% from the mean

value, since the mean value also contains the trigger errors.

$R_n I_c$ of J_2

The product of R_n and I_c in a JJ in the long regime, namely that the junction length is larger than the superconducting coherence length (ξ_s), is proportional to the Thouless energy (E_{th}).^{5,6} This energy is inversely proportional to the time (τ) that a charge carrier spends in the junction, i.e. the graphene. For a ballistic junction $E_{th} = \hbar v_F/L$, where L the junction length.

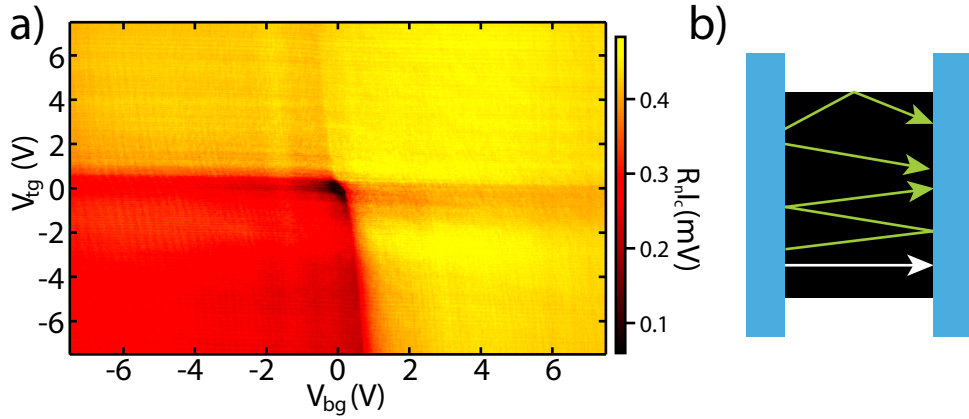


Figure S3: a) Product of R_n and I_c as a function of V_{tg} and V_{bg} . If both layers are n doped we observe a value of 0.4 mV. This value reduces to 0.25 mV, if both layers are p doped. b) Schematic drawing of a Josephson junction and possible ballistic trajectories of the supercurrent carrying channels. The superconducting leads are indicated by blue, while the graphene is black. The white arrow corresponds to the shortest trajectory between the leads, while scattering at the physical edge of the graphene, reflection at the imperfect contacts or a finite angle distribution can lead to increased length of the paths.

$R_n I_c$ for J_2 is shown in Fig.S3 a. We observe a constant value in each quadrant apart the DPs, i.e. nn, np, pn, and pp, for the product, which indicates a constant value of E_{th} . Nevertheless, the value never reaches the expected one of 1 mV given by $v_F = 10^6$ m/s for graphene and the junction length $L = 650$ nm. This points into the direction, that the superconducting path decohere stronger than expected. Further, $R_n I_c$ varies between the different quadrants. While it is equal to 0.4 mV, if both layers are n doped, it decreases to 0.25 mV in the pp regime. This points into the direction that the imperfect contacts

are leading to a suppression of E_{th} . This can be seen as the charge carrier are spending an effectively longer time than L/v_F in the junction, which can be due to reflection at the contacts or the physical graphene edges (see Fig.S3 b).

Suppressed resistance in moderate out-of-plane magnetic fields

At magnetic fields large enough to suppress the supercurrent in the JJ but smaller than the field needed to be in the quantum Hall (QH) regime, irregular oscillations of the resistance around zero dc-current bias are observed (see Fig.S4). The gate voltages were set to $V_{bg}=-1.5$ V and $V_{tg}=1.5$ V, while the resistance as a function of out-of-plane magnetic field (B_z) was measured with a standard lockin technique. The ac-current amplitude was set to 50 pA. The appearance of these random oscillations were already observed by Ben Shalom et al.⁷ and are attributed to the ballistic transport nature of the junction, which leads to billiard like trajectories at the edges of the sample. These trajectories are suspected to form irregularly Andreev states, while the ones in the bulk are fully suppressed by the magnetic field. Therefore, it is another indication of the ballistic transport nature of J_2 . Nevertheless, the observation of this superconducting pockets disappears at fields larger than 440 mT and were not observed in the QH regime within our resolution of 50 pA as shown in Ref.⁸

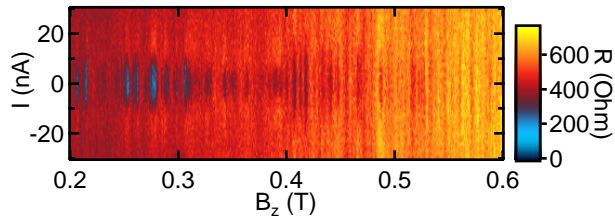


Figure S4: Resistance as a function of current bias and out-of-plane magnetic field. A suppression of the resistance around 0 nA bias current was observed up to fields of 440 mT.

Calibration and alignment of the in-plane magnetic field

To measure the in-plane magnetic field dependence of such a DLG SQUID device, one has to carefully calibrate and adjust the direction of the magnetic field. Due to the large ratio between the JJs area and the area of the SQUID loop, e.g. 1:35 for J_2 , the I_c^i of each JJ is more sensitive to an out-of-plane magnetic field than I_c of the SQUID to an in-plane field. If the alignment is imperfect, which results in a finite out-of-plane component, the SQUID interference pattern decays due to the interference of the supercurrent in the individual junctions. Further we will show that also a component x-direction (see Fig.S5 c) leads to a reduction in I_c as well.

The calibration was performed using a 3D vector magnet with the magnetic fields B_1 , B_2 , and B_3 , which are perpendicular to each other. While the graphene plane was roughly lying in the plane of the first and second magnet with B_1 and B_2 , the magnetic field of the third one is pointing out-of-plane. In a first step we had to measure three different points, which are in the xy-plane of the sample. This was done by setting the values of the first and second magnet to the values given in the inset of Fig.S5 a. At each point the out-of-plane magnetic field (B_3) was swept and a Fraunhofer like interference pattern was measured. The point in B_3 , where I_c is maximal reflects the best compensation of the out-of-plane magnetic field, i.e. correspond to a magnetic field in the plane of the JJs. With these three point we defined two vectors, which have to lie in-plane of the graphene layers. To define now a coordinate system we took the cross product of these two vectors to obtain the normal vector \vec{n} of the plane. Then one of the original vectors was normalized and defined as the temporally x-axis (\vec{e}_x). By taking now the cross product of \vec{e}_x and \vec{n} we obtain the unit vector in y-direction (\vec{e}_y). The two unit vectors \vec{e}_x and \vec{e}_y span now the plane of the graphene layers and allows us to sweep the magnetic field in this plane. Notice, that the direction of the defined vectors are arbitrary and not related to any alignment with the device, e.g. contacts, yet. To find calibrate the magnetic field direction with respect to the device structure, we rotated the magnetic field from -360° to 360° for two different magnitudes (see Fig.S5 b).

Curves with a periodicity of 180° were observed as expected, but the origin of their shape was not fully clear in the beginning. Therefore the magnetic field direction was fixed at an angle of a maxima of either curve shown in Fig.S5 b. By sweeping the magnitude of the magnetic field in these two direction we observed the interference pattern plotted in Fig.S5 c and d, from which we could determine the in-plane field direction perpendicular to the SQUID (B_y). Notice, that I_c also strongly depends on the magnitude of the magnetic field which is applied parallel to the SQUID's cross section, i.e. in supercurrent direction. This suppression by B_x is attributed to the Meissner effect, which expels the magnetic field out of the superconducting contact leading to a finite and inhomogeneous out-of-plane magnetic field through the graphene planes. In the direction of B_y we find the modulation of I_c typical for a SQUID. A small decay of the maximal value is observed at higher fields.⁹ This can either come from a magnetic field component in x or z-direction due to an imperfect alignment or due to out-of-plane corrugations of the individual graphene layers.^{10,11}

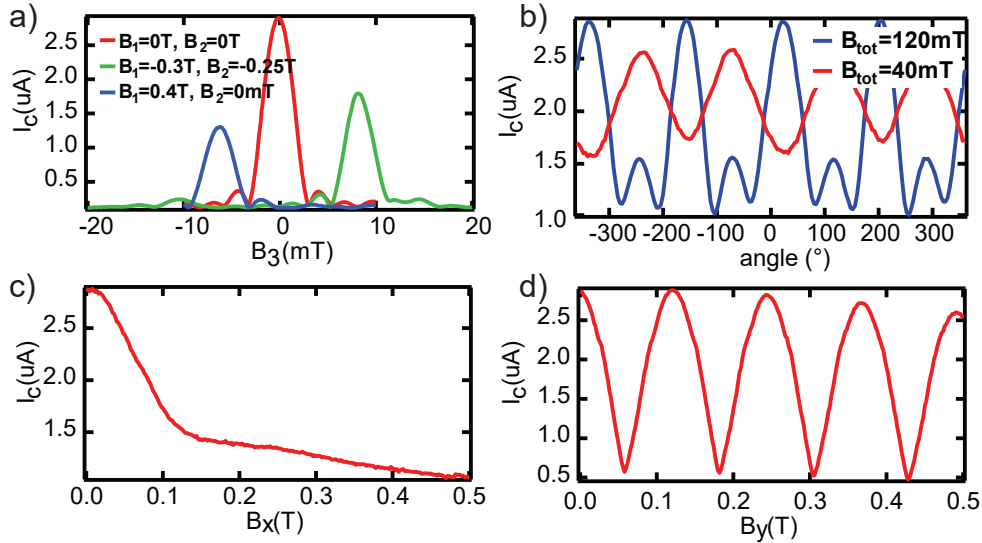


Figure S5: a) Critical current as a function of B_3 for three pairs of B_1 and B_2 . b) Critical current as a function of the direction of the in-plane field for two fixed magnitudes of the in-plane magnetic field. c) Dependence of the critical current as a function of B_x . d) Critical current as a function of B_y .

To obtain the CPR, we subtracted the average of I_c over one period for every value of n_i and B , which corresponds to the switching current of the reference junction. This leaves us

with the CPR.

Minima of $I_c(B_y)$ as a function of V_{tg}

For a symmetric SQUID ($I_c^1 = I_c^2$) with a sinusoidal CPR, one expects a $|\cos(\pi\Phi/\Phi_0)|$ like interference pattern of I_c vs magnetic field. Therefore one would observe that I_c fully vanishes at a magnetic flux equal to $\Phi_0/2$. If the SQUID is not symmetric, the supercurrent flowing in the two JJs will not fully compensate each other at $\Phi_0/2$, leaving us with a finite I_c . But this observation is also possible if the CPR is not sinusoidal, even if the JJs are symmetric. To show that the non vanishing I_c in the interference pattern in Fig.3 d of the article, is not only due to an asymmetry of the JJ, but rather given by a non sinusoidal CPR, we measured I_c as a function of V_{tg} , while V_{bg} was fixed at 5 V and the in-plane magnetic field at -181.6 mT, which corresponds to a minimum of the interference pattern (see Fig.S5). When V_{tg} is tuned mainly the critical current carried by the top graphene layer changes. Like this it is possible to change between a symmetric and an asymmetric SQUID configuration. At the DP of the top layer ($V_{tg} \approx 0$ V) the supercurrent is carried only by the bottom layer and the critical current is therefore only given by I_c^b . When the gate voltage is increased, I_c^t also increases. Since there is a phase difference of roughly $\pi/2$ between the JJs due to the magnetic flux, the supercurrent flows in the opposite direction, which leads to a decrease of SQUID's I_c . This trend continues until $I_c^t = I_c^b$, where I_c will reach its minimum before it starts to increase again due to opposite asymmetry ($I_c^t > I_c^b$). The non zero I_c in the symmetric SQUID is attributed to the non sinusoidal CPR observed and discussed in the main text. This can be seen by taking a look how I_c as a function of B is calculated. First, the total supercurrent is given by $I_c = I_c^t f^t(\varphi_t) + I_c^b f^b(\varphi_b)$, where φ_t (φ_b) is the phase difference over the top (bottom) JJ and $\varphi_t = \varphi_b + \pi\Phi/\Phi_0$. For a given magnetic field $\varphi_t - \varphi_b$ is fixed but not the value of φ_b . To obtain now I_c one has to maximize I_c over φ_b . Therefore, to obtain a I_c of zero, I_c has to be zero for all φ_b . This is the case for the sum of two sinus curves shifted by $\pi/2$ but is never the case if the CPRs are skewed sinusoidal functions. Therefore, the non vanishing

supercurrent can be attributed to a non sinusoidal CPR.

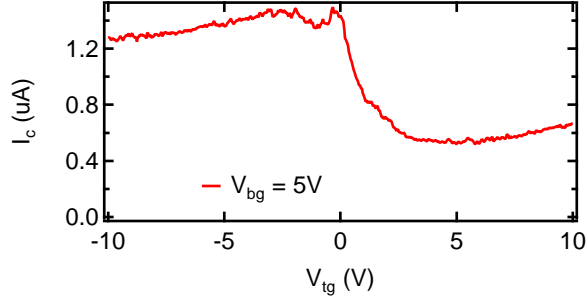


Figure S6: I_c as a function of V_{tg} for $V_{bg}=5$ V. The critical current was measured for a in-plane magnetic field (B_y) of -181.6 mT.

Gate dependence of a_n

To fit the CPR we used Eq.3 in the article, which contains up to the fifth harmonic in frequency. If the CPR is sinusoidal a_2 to a_5 are all zero and only the first harmonic exists. The non-vanishing of the higher harmonic amplitudes indicates, that the CPR will be skewed and can be used as an alternative measurement quantity to the skewness (see main text) to define the deviation of the CPR from the sinusoidal behavior. For completion, we plot the a_1 to a_3 and the ratio between a_2 and a_1 , as well as the ratio between a_3 and a_1 in Fig.S7. The amplitudes a_4 and a_5 are much smaller than the the others and their contribution to skewness of the CPR can be neglected. For n (p) doped graphene a skewness of 0.25 (0.15) was extracted. This value corresponds to a ratio of a_2/a_1 of around 0.15 (0.1).

Calculation of the interference pattern

To get an idea of the asymmetry of the measurement shown in Fig.3 d of the main article, we calculated the in-plane magnetic field dependence of the I_c . The CPRs were chosen to be equal and with skewness of $S=0.18$, which is given by the choice of the prefactors a_1 , a_2 , and a_3 in Eq. 3 of the main text. The blue curve is the result of $I_c^b = 1.2 \mu\text{A}$ and $I_c^t = 0.6 \mu\text{A}$,

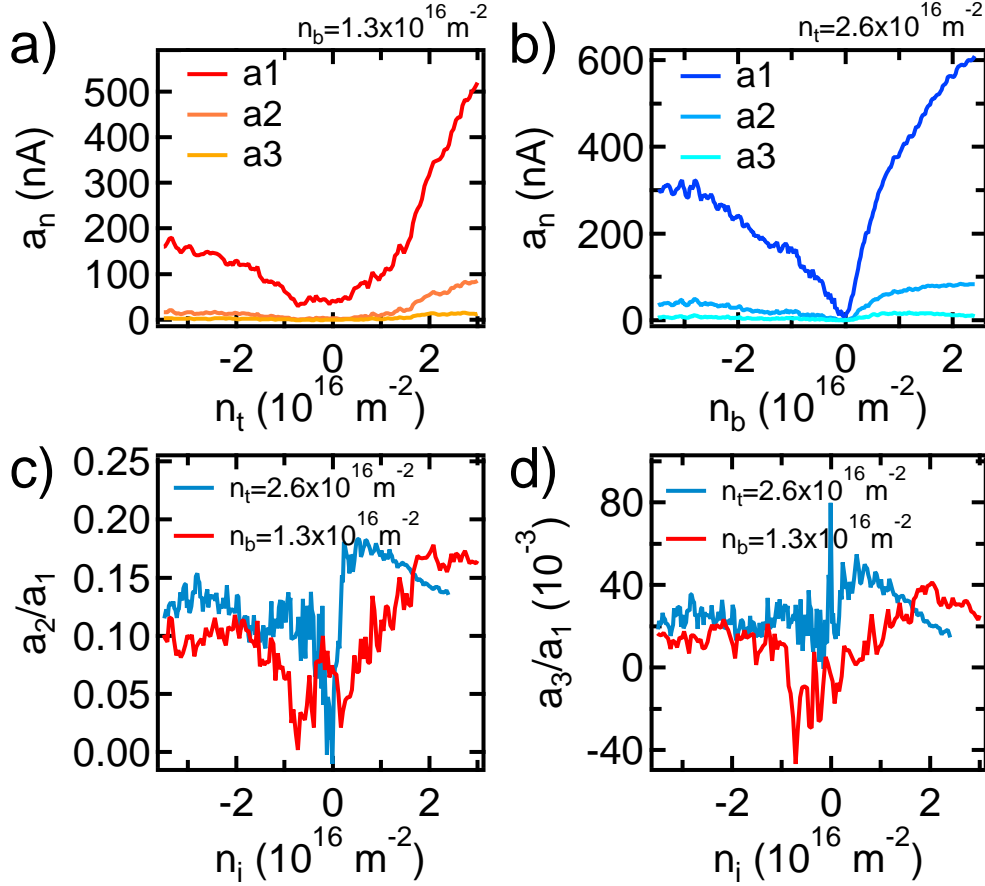


Figure S7: a) Fitting coefficients a_1 , a_2 , and a_3 as a function of n_t for $n_b=1.3\times 10^{-2}$. b) Fitting coefficients a_1 , a_2 , and a_3 as a function of n_b for $n_t=2.6\times 10^{-2}$. c) Ratio of a_2 and a_1 , which are shown in a) and b). d) Ratio of a_3 and a_1 , which are shown in a) and b).

the red one for $I_c^b = 1.4 \mu\text{A}$ and $I_c^t = 1.4 \mu\text{A}$ and the green for $I_c^b = 2 \mu\text{A}$ and $I_c^t = 1.4 \mu\text{A}$. For the blue result we took the dimension (junction length and middle hBN thickness) of J_1 , for the red the dimension of J_2 , and for the green curve the dimension of J_3 . The result reproduces qualitatively the measurements in Fig.S8 b). Therefore, we conclude that the in-plane magnetic field dependence of J_2 was in a rather symmetric state of the SQUID, while for J_1 and J_3 the SQUID was slightly asymmetric. The calculations also reproduce the shape of the different curves.

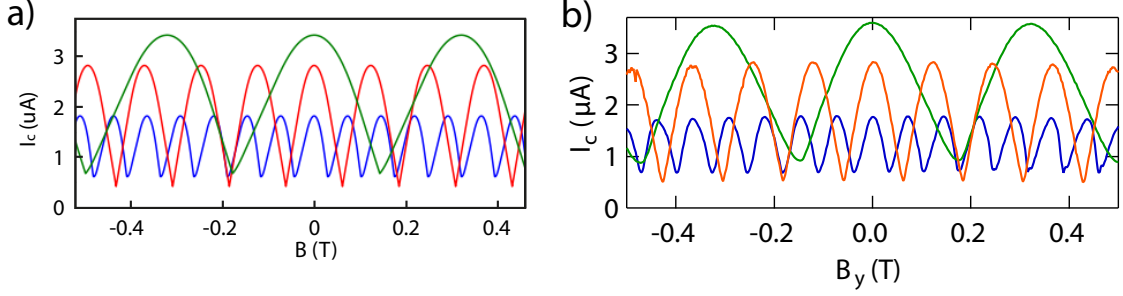


Figure S8: a) Calculated interference pattern for a SQUID with a skewed CPR ($S=0.18$). The different curves, indicated by different colors, were obtained for different SQUID areas, which corresponds to the ones of J_1 (blue), J_2 (red) and J_3 (green). b) Measurement of the critical current as a function of in-plane magnetic field for J_1 , J_2 , and J_3 .

Estimation of the loop inductance

The loop inductance (L_s) can lead to screening of the external magnetic field, which modifies the actual flux (Φ) inside the SQUID. Further it makes the relation between Φ and the external flux (Φ_{ext}) non linear. When the magnetic field axis is converted to a phase axis, this non linearity has to be taken into account, if L_s or I_c is large. In the case of a symmetric dc-SQUID, Φ_{ext} as a function of Φ can be expressed by

$$\Phi_{ext} = \Phi + L_s I_c f \left(\frac{\pi \Phi}{\Phi_0} \right). \quad (15)$$

Further, L_s and I_c defining the limit, at which the phase biasing by a magnetic field gets hysteretic. This limit is given by $\pi L_s I_c / \Phi_0 \approx 1$. To estimate the loop inductance, we calculated the kinetic inductance (L_k) of the MoRe leads and the geometric inductance (L_g) of the SQUID loop. The sum of these inductances results in L_s .

L_k was measured by the temperature dependence of the resonance frequency (f_{res}) of a $\lambda/4$ -resonator.

$$f_{res} = \frac{1}{4l \sqrt{\left(L_m + \frac{L_k^0}{1 - \left(\frac{T}{T_c} \right)^4} \right) \cdot C_m}}, \quad (16)$$

where l is the length of the resonator and L_k^0 is the kinetic inductance per unit length

in the zero temperature limit. The geometric inductance of the resonator (L_m) as well as the geometric capacitance of the resonator (C_m) were calculated as described in Ref.¹² We obtain a sheet inductance of $L_k^s=4.26$ pH for a resonator thickness of 70 nm. L_k is obtained by multiplying the sheet inductance with the interlayer distance, here $d_{gg}=25$ nm, and divide it by the the contacts width of 550 nm. By doing so $L_k=0.19$ pH. Note, that this is an upper bound of the kinetic inductance, since the L_k^s was determined using a 70 nm thick resonator. Here, due the supercurrent direction the thickness would correspond to the length of the contact region, which is about 850 nm. Therefore, we expect the kinetic inductance to be even smaller.

To estimate L_g we calculate the inductance of a rectangular loop as derived in Ref.¹³ Here we take the following values: $l_1=L$, $l_2 = d_{gg}$, $w=0.3$ nm (thickness of graphene) and $h=1$ nm the width of the of the loop. By taking h equal to only 1 nm instead of the entire junction width, we get an upper limit of the geometrical inductance of $L_g=1.2\times 10^{-12}$ H. This has to be done since the used formula does not hold if h is much larger then the product of l_1 and l_2 .

We calculate now the difference between Φ_{ext} and Φ at $\Phi = \Phi_0/2$, where the effect of the screening is the strongest. For a critical current of $3 \mu\text{A}$, the difference is not more then 0.3%. Further, the maximal current, which can be passed through the SQUID before it starts to behave hysteretic is $I_c^h \approx 0.5$ mA. For these reasons screening effects can be neglected in our measurements, since the measured critical currents are way smaller and the non linearity is not present.

References

- (1) Ni, Z. H.; Wang, H. M.; Kasim, J.; Fan, H. M.; Yu, T.; Wu, Y. H.; Feng, Y. P.; Shen, Z. X. Graphene thickness determination using reflection and contrast spectroscopy. *Nano Letters* **2007**, *7*, 2758–2763.

- (2) Zomer, P. J.; Guimaraes, M. H. D.; Brant, J. C.; Tombros, N.; Van Wees, B. J. Fast pick up technique for high quality heterostructures of bilayer graphene and hexagonal boron nitride. *Applied Physics Letters* **2014**, *105*, 1–4.
- (3) Indolese, D. I.; Delagrangé, R.; Makk, P.; Wallbank, J. R.; Watanabe, K.; Taniguchi, T.; Schönenberger, C. Signatures of van Hove Singularities Probed by the Supercurrent in a Graphene-hBN Superlattice. *Physical Review Letters* **2018**, *121*, 137701.
- (4) Handschin, C.; Makk, P.; Rickhaus, P.; Liu, M. H.; Watanabe, K.; Taniguchi, T.; Richter, K.; Schönenberger, C. Fabry-Pérot resonances in a graphene/hBN Moiré superlattice. *Nano Letters* **2017**, *17*, 328–333.
- (5) Borzenets, I. V.; Amet, F.; Ke, C. T.; Draelos, A. W.; Wei, M. T.; Seredinski, A.; Watanabe, K.; Taniguchi, T.; Bomze, Y.; Yamamoto, M.; Tarucha, S.; Finkelstein, G. Ballistic Graphene Josephson Junctions from the Short to the Long Junction Regimes. *Physical Review Letters* **2016**, *117*, 1–5.
- (6) Dubos, P.; Courtois, H.; Pannetier, B.; Wilhelm, F. K.; Zaikin, A. D.; Schön, G. Josephson critical current in a long mesoscopic S-N-S junction. *Physical Review B* **2001**, *63*, 1–5.
- (7) Ben Shalom, M.; Zhu, M. J.; Fal’ko, V. I.; Mishchenko, A.; Kretinin, A. V.; Novoselov, K. S.; Woods, C. R.; Watanabe, K.; Taniguchi, T.; Geim, A. K.; Prance, J. R. Quantum oscillations of the critical current and high-field superconducting proximity in ballistic graphene. *Nature Physics* **2016**, *12*, 318–322.
- (8) Amet, F.; Ke, C. T.; Borzenets, I. V.; Wang, Y.-M.; Watanabe, K.; Taniguchi, T.; Deacon, R. S.; Yamamoto, M.; Bomze, Y.; Tarucha, S.; Finkelstein, G. Supercurrent in the quantum Hall regime. *Science* **2016**, *352*, 966–969.
- (9) Steinigeweg, R.; Jin, F.; Schmidtke, D.; De Raedt, H.; Michielsen, K.; Gemmer, J.

Real-time broadening of nonequilibrium density profiles and the role of the specific initial-state realization. *Physical Review B* **2017**, *95*, 1–6.

- (10) Couto, N. J.; Costanzo, D.; Engels, S.; Ki, D. K.; Watanabe, K.; Taniguchi, T.; Stampfer, C.; Guinea, F.; Morpurgo, A. F. Random strain fluctuations as dominant disorder source for high-quality on-substrate graphene devices. *Physical Review X* **2014**, *4*, 1–13.
- (11) Kim, Y.; Herlinger, P.; Taniguchi, T.; Watanabe, K.; Smet, J. H. Reliable Postprocessing Improvement of van der Waals Heterostructures. *ACS Nano* **2019**, *13*, 14182–14190.
- (12) Gevorgian, S. Basic characteristics of two layered substrate coplanar waveguides. *Electronics Letters* **1994**, *30*, 1236–1237.
- (13) Shatz, L. F.; Christensen, C. W. Numerical Inductance Calculations Based on First Principles. *PLoS ONE* **2014**, *9*.